

# Substructures in the MACSIS hydrodynamical simulation of galaxy clusters

Edoardo Altamura\*

PHYS 40181  
MPhys Thesis

Supervisor: Dr Scott Kay  
Project collaborator: Martin Murin

January 6, 2019

## Abstract

Using the MAssive ClusterS and Intercluster Structures (MACSIS) simulations, the substructures populating large galaxy clusters were identified using the SUBFIND algorithm and analysed, in the case of Dark-Matter-Only (DMO) halos and in that including hydrodynamics (HYDRO), in addition to subgrid processes. The 10 most massive MACSIS clusters, evolved to the present redshift, revealed a larger abundance of substructures with masses  $M_{sub} < 10^{13} M_{\odot}$  in the DMO simulation than in the HYDRO run. Such effect, associated to the contribution of baryons, was confirmed by the subhalo density profiles, which indicated a larger density of HYDRO substructures close to the centre of potential of the host cluster. NFW model fits, applied to the combined DMO and HYDRO clusters' median density profiles, delivered an average concentration of  $4.93 \pm 0.09$  and  $5.51 \pm 0.18$  respectively, explained by the action of dissipative processes. Moreover, the mass fractions of the HYDRO substructures highlighted the absence of gas in objects with  $M_{sub} < 10^{13} M_{\odot}$ , which may have been subject to ram pressure stripping in entering the intra-cluster medium, while leaving the stellar and dark matter components unchanged. The baryon fraction was instead gas-dominated for  $M_{sub} > 10^{13} M_{\odot}$ , reflecting more massive substructures outside the virial radius of the clusters. Ultimately, the velocity distribution and considerations on the bulk motion of subhalos are reported for the largest of the 10 MACSIS clusters, indicating a close agreement between the DMO and HYDRO (dark matter and stars) datasets for both the line-of-sight and the physical velocity. The kinematic analysis will constitute a crucial section in the second part of the project, focused on the kinetic Sunyaev-Zel'dovich effect on galaxy cluster substructures.

**Key words:** galaxies: clusters: general - methods: numerical - hydrodynamics - galaxies:  
clusters: substructures - galaxies: clusters: MACSIS

---

\*Email: [edoardo.altamura@student.manchester.ac.uk](mailto:edoardo.altamura@student.manchester.ac.uk)

## 1 Introduction

Galaxy clusters are the astronomical objects constituting the nodes of the cosmic web and other large scale structures of the Universe (Blumenthal et al., 1984; Bond et al., 1996; Allen et al., 2011). They originated from primordial density fluctuations, which then evolved over time via processes of gravitational accretion and feedback (van Albada, 1961; Doroshkevich et al., 1983; Blumenthal et al., 1984; Davis et al., 1985). The most widely accepted theoretical framework for the generation of such fluctuations is known as  $\Lambda$ -Cold Dark Matter ( $\Lambda$ CDM) model (Kompaneets et al., 1981; Blumenthal et al., 1984; Efstathiou et al., 1988). Given an initial mass distribution, the  $\Lambda$ CDM model postulates that the gravitational interaction between particles gives rise to hierarchical clustering of structures, according to which larger objects form from the merging of smaller structures (White & Frenk, 1991; Katz & White, 1993; Aragon-Calvo & Szalay, 2013). Within such *bottom-up* scenario, galaxy clusters are therefore key in probing the dynamics of structure formation in the Universe, inferring the cosmological parameters and narrowing the constraints for the validity of the  $\Lambda$ CDM paradigm.

In order to translate the predictions of the  $\Lambda$ CDM into observables to be compared against experimental data,  $N$ -body simulations have first been developed by von Hoerner (1960), who implemented integration algorithms up to  $N = 16$  for investigating the relation between relaxation time and age of clusters. The quest for a larger number of simulated particles soon became a crucial drive for constructing more efficient and highly scalable algorithms, with the aim of performing accurate studies of the largest galaxy clusters observed (Aarseth, 1963, 1966, 1969; Aarseth & Hoyle, 1964; Aarseth et al., 1979). Over the last decades, numerous integration methods have been constructed and tested, including the Kustaanheimo-Stiefel regularisation (Kustaanheimo & Stiefel, 1965; Chernyagin & Lezhnin, 2015) and their Hamiltonian implementations (Peters, 1968; Mikkola & Tanikawa, 1999a,b), until the introduction of *tree codes*, owed to Barnes & Hut (1986a) and further described in section 2.1. The simulation code used for this work is GADGET-3, a suite of C language routines embedding the  $\Lambda$ CDM model for computing Smoothed Particle Hydrodynamics (SPH) and gravity simulations in a cosmological context (Springel et al., 2001a; Springel, 2005; Evrard, 1988). The Lagrangian TreePM-SPH version of GADGET-3 code was implemented by Barnes et al. (2015, 2017) in the MAssive ClusterS and Intercluster Structures (MACSIS) project, involving the simulation of a  $(3.2 \text{ Gpc})^3$  volume and the identification of 390 clusters via the Friends-of-Friends (FoF) algorithm (Davis et al., 1985).

The main subjects of this study are the substructures formed within the halos in the MACSIS sample, which were post-processed using the SUBFIND algorithm, in order to detect the presence of smaller satellite objects (Springel et al., 2001b; Dolag et al., 2009). Details on the applications and results of the SUBFIND methodology can be found in section 2.3. Not only is the study of galaxy clusters crucial in testing cosmological models on large scales, but also allows smaller objects to be investigated under a new light. In fact, according to Moore et al. (1999); Ghigna et al. (2000); Springel et al. (2001b); Stoehr et al. (2002) and De Lucia et al. (2004), the  $\Lambda$ CDM hierarchical clustering supports the formation of substructures within massive clusters of galaxies, which are tightly linked to the environment in which they evolve. The information deriving from the analysis of substructures can be used to further constrain the overall properties of the host cluster, allowing more accurate assessment of weak and strong lensing observations (Allen et al., 2011; Jauzac et al., 2018; Cramer et al., 2018; Pandge et al., 2019; Plazas et al., 2019), Sunyaev-Zel'dovich (SZ) signal characterisation (Allen et al., 2011; Mayet et al., 2017; Adam et al., 2017; Pandge et al., 2019; Di Mascolo et al., 2018; Lopes et al., 2018; Adam et al., 2018) and dynamical maps from redshift surveys (Davis & Peebles, 1983; Baugh & Efstathiou, 1994; Peacock et al., 2001; Beutler et al., 2011).

The present work develops in two main parts: the matter distribution of substructures and their dynamical properties. Both are introduced by section 2, which illustrates the theoretical

framework for the simulation and structure formation, in addition to the processing stages of the data pipeline for the MACSIS sample. Subsequently, section 3 focuses on the static mass distribution of substructures, preluding to the kinematic analysis, contemplated in section 4. Ultimately, the major results are summarised and discussed in section 5, where an outline of related future research concludes the thesis.

## 2 Theory and simulations

Modern  $N$ -body cosmological simulations are developed using two main classes of code routines, including numerical solvers for gravitational interactions and hydrodynamic processes. Both can be modelled by an ensemble or point-like particles, which act as tracers of mass. In order to readily disentangle the overall effects of gravity and hydrodynamics, two versions of the simulations are often produced: the Dark-Matter-Only (DMO) simulation, resulting from the dynamics of non-baryonic mass-tracing particles excluding baryonic hydrodynamics, and the hydrodynamical (hereafter HYDRO) simulation, comprising both baryonic and non-baryonic particles.

In accordance with Blumenthal et al. (1984) and Davis et al. (1985), cold dark matter can be regarded as a collisionless fluid, only subject to gravitational forces. Consequently, its time evolution can be described by the *collisionless Boltzmann equation*, which reads

$$\frac{df}{dt} = \frac{\partial f}{\partial t} + \dot{\mathbf{r}} \cdot \nabla f - \nabla \Phi \cdot \frac{\partial f}{\partial \dot{\mathbf{r}}} = 0, \quad (1)$$

where the phase-space density function  $f \, d\mathbf{r} d\dot{\mathbf{r}} dt \equiv f(\mathbf{r}, \dot{\mathbf{r}}, t) \, d\mathbf{r} d\dot{\mathbf{r}} dt$  expresses the normalised probability of finding a randomly chosen particle of given mass within the box  $\mathbf{r} + d\mathbf{r}$  and moving with velocity between  $\dot{\mathbf{r}} + d\dot{\mathbf{r}}$  in the time interval  $t + dt$ . The solution of equation 1 depends on the form of the potential  $\Phi(\mathbf{r})$ , which can be computed by solving Poisson's equation for  $f$  (Springel et al., 2001a; Dehnen & Read, 2011). The validity of the Newtonian approximation for gravity simulations has been justified by Cooperstock et al. (1998), who showed that the general relativistic corrections are minimal at the densities and scales of galaxy clusters.

The second class of processes involves the modelling of the intracluster medium (ICM) as an ideal gas, subject to the equation of state  $P = (\gamma - 1)u\rho$ , relating the pressure  $P$  of the gas to its energy per unit mass  $u$ , the mass density  $\rho$  and the adiabatic exponent  $\gamma$ , to be adjusted according to the different chemical species of gas introduced in the system. Differently from the case of gravity interactions, the hydrodynamics is developed from the equations of a collisional fluid, often approximated to have zero viscosity (Springel et al., 2001a; Springel, 2005; Dolag et al., 2005). Under such assumptions, the evolution of the ICM is governed by the continuity equation and Euler's equation, respectively in the form of

$$\frac{d\rho}{dt} + \rho \nabla \cdot \dot{\mathbf{r}} = 0 \quad \text{and} \quad \ddot{\mathbf{r}} + \frac{1}{\rho} \nabla P + \nabla \Phi = 0, \quad (2, 3)$$

combined with the first law of thermodynamics

$$\frac{du}{dt} + \frac{P}{\rho} \nabla \cdot \dot{\mathbf{r}} + \frac{\Lambda(u, \rho)}{\rho} = 0 \quad (4)$$

adapted to account for additional astrophysical processes, such as radiative cooling, photoionisation, chemical species and thermal feedback, included in the term in  $\Lambda(u, \rho)$  (Springel et al., 2001a; Springel, 2005). Further information regarding the form of  $\Lambda(u, \rho)$  for the individual processes implemented in the simulation code can be found in Katz et al. (1996); Springel (2000); Yoshida et al. (2003); Kay et al. (2004), as well as Hayward et al. (2014).

The partial differential equations for gravity and hydrodynamics constitute the theoretical

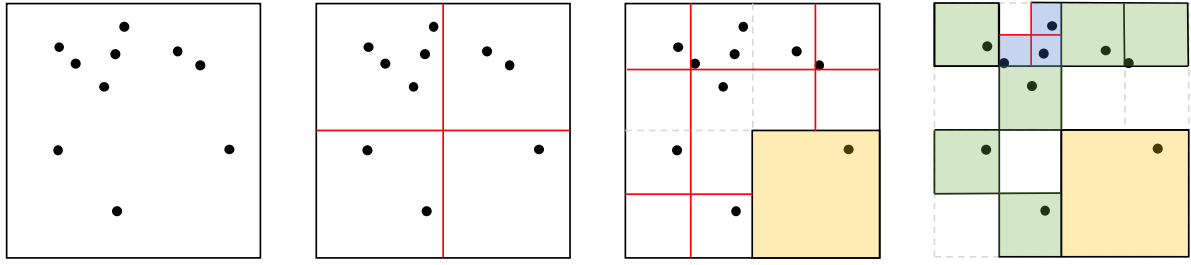


Figure 1: Illustration of the TreePM method applied in a 2-dimensional space. The iterations of the algorithm are ordered from left to right, with the red lines displaying the subdivision of spaces into quadrants. For each quadrant, the subdivision is interrupted when the Hilbert-Peano sampling returns one single particle in the domain region. In the example above, the yellow-shaded regions are fully sampled after one iterations, followed by the green and blue-shaded regions.

framework for the development of the simulation, achieved using the numerical methods, initial conditions and boundary conditions illustrated in section 2.1.

## 2.1 The Lagrangian TreePM-SPH GADGET-3 code

The first attempts at solving equations 1-4 showed difficulties in reproducing simulations with larger number of particles,  $N$ , using direct methods of integration (von Hoerner, 1960; Aarseth, 1963, 1966, 1969; Aarseth & Hoyle, 1964; Aarseth et al., 1979; Kustaanheimo & Stiefel, 1965; Chernyagin & Lezhnin, 2015). Such  $N$ -scalability barrier has been overcome by the introduction of Tree and Particle-Mesh (PM) codes, requiring computational resources of order  $\mathcal{O}(N \log N)$  and  $\mathcal{O}(N)$  respectively, instead of order  $\mathcal{O}(N^2)$ , typical of pairwise algorithms (Springel et al., 2001a; Springel, 2005; Hayward et al., 2014). The GAlaxies with Dark matter and Gas intEract (GADGET) code, developed and reviewed by Springel (2005), implements both methods for the computation of dark matter particles and baryonic physics. Given a set of point-like particles in a 3-dimensional cube, the TreePM method consists in subdividing the volume into a grid of 8 identical octants. The particles in each octant are then sampled using a Hilbert-Peano curve, before further subdividing each octant according to the number of particles detected by the sampling algorithm. This process is repeated until a hierarchical mesh is produced, as showed in figure 1. The advantage of such algorithm lies in the sampling only of the regions populated by particles, which are grouped more finely as the algorithm advances. Furthermore, the TreePM output intervenes in the calculation of gravitational forces, retaining the coarse particle grouping for long-range forces, while allowing higher accuracy and fine subdivisions for short-range interactions, leading to the  $\mathcal{O}(N \log N)$  scalability relation mentioned above. The computation of the particle mesh is adaptive to any particle distribution and boundary condition, which is chosen to be periodic in the case of GADGET (Appel, 1985; Porter, 1985; Barnes & Hut, 1986b; Jernigan & Porter, 1989; Springel et al., 2001a).

Figure 1 also suggests that regions with lower density of particles are associated with larger domain regions, whose size is known as *smoothing length*. Due to such feature, the TreeMP algorithm fills the domain with regions having different smoothing lengths, allowing the modelling of continuous media, such as gas, using a distribution of smoothed particles, mathematically represented by Dirac  $\delta$ -functions convoluted with the spline introduced by Monaghan & Lattanzio (1985). This convolution method defines the Lagrangian Smoothed Particle Hydrodynamics (SPH) adopted in GADGET. The TreePM method also proved to be equally efficient in the computation of gravitational interactions, provided that very close encounters between particles do not result in unrealistically large momentum scatter Hernquist & Katz (1989). In order to mitigate the particle scatter in high density region, Plummer (1911) proposed a modified form

for the single-particle Newtonian potential:

$$\Phi(r) = -G \frac{m}{r + \epsilon}, \quad (5)$$

where  $m$  is the mass of the particle and  $\epsilon$  the Plummer softening scale, set to  $4 h^{-1}\text{kpc}$  in the case of the final version of the MACSIS project, and  $h$  is the Hubble parameter (Barnes et al., 2017).

The initial conditions are represented by the power spectrum and cosmological parameters reported by Planck Collaboration et al. (2014a,b), simulated from a redshift  $z = 127$ , selected in compliance with the Zel'dovich approximation for structure formation (Zel'dovich, 1970; Peebles, 1980; White, 2014).

## 2.2 The MACSIS sample

The Lagrangian TreePM-SPH GADGET-3 version of the code was used to simulate  $N = 2520^3$  DMO particles enclosed within a  $(3.2 \text{ Gpc})^3$  cubic volume with periodic boundary conditions, in agreement with the framework described in section 2.1. Using the computational facilities available at the Virgo Consortium, the simulation was run up to the present redshift, when the result was transferred to the Friends-of-Friends (FoF) routine (Davis et al., 1985), in order to identify the clusters of particles, representing the halos of galaxy clusters. The FoF algorithm samples the pairs of particles which are closer than a distance defined by the linking length parameter  $b$ , set to 0.2 by Barnes et al. (2017). If the particles, each with mass  $m = 8.012 \times 10^{10} M_\odot$ , are closer than the linking length, the algorithm connects them, growing a network that ultimately defines the *FoF halos* or *FoF groups*.

The MACSIS sample was constructed by dividing the FoF groups in mass bins, ranging over  $10^{15.0} M_\odot \leq M_{\text{FoF}} \leq 10^{15.8} M_\odot$ , and selecting the 390 largest groups. The simulation of the vast  $(3.2 \text{ Gpc})^3$  volume, defined as *parent simulation*, guaranteed a large enough domain to be able to identify objects representing the largest galaxy clusters in the observable universe, which are proved to be statistically much rarer than lower mass clusters (Jenkins et al., 2001; Vikhlinin et al., 2009). At a later stage, smaller volumes centred on each of the 390 clusters were simulated using the same framework, although with increased resolution ( $\epsilon$  reported in earlier sections and DMO particle mass  $m_{DM} = 7.40 \times 10^9 M_\odot$ ) and with the addition of the SPH hydrodynamical routines, involving particles of mass  $m_{gas} = 1.18 \times 10^9 M_\odot$  (Katz & White, 1993; Tormen et al., 1997; Barnes et al., 2017) and surrounding tidal forces from the cosmic web. Such technique, known as *zoom simulation* was used to provide grater detail in the DMO and HYDRO versions of the MACSIS run, allowing simpler comparison with results from previous projects (McCarthy et al., 2017), as well as the possibility to probe the properties of substructures, also named *subhalos* or *subgroups*, populating the FoF objects.

Crucially, the MACSIS objects and their subhalos were modelled using additional subgrid physics implemented in TreePM-SPH GADGET-3, including stochastic star formation (Schaye & Dalla Vecchia, 2008), feedback from supernovae, active galactic nuclei and stellar winds (Dalla Vecchia & Schaye, 2008; Booth & Schaye, 2009), as well as updated methods for chemical elements information, interpolation and free parameter tuning (Schaye et al., 2010; Le Brun et al., 2014; McCarthy et al., 2017; Barnes et al., 2017). In agreement with the hierarchical structure formation introduced in section 1, the largest MACSIS clusters are the result of multiple interactions with smaller objects, with the consequence of them being non-virialised and dynamically active even at  $z = 0$ . Such processes strongly influence the morphology, structure and baryon content of galaxy cluster, as extensively studied by Henson et al. (2017), rendering them the ideal environment for the analysis of substructures. Major mergers are the central topic of this work, which will include the analysis of the 10 most massive MACSIS halos, numbered progressively in order of decreasing mass and labelled by the FoF number  $n_{\text{FoF}} \geq 0$ .

### 2.3 Post-processing with SUBFIND

The DMO and HYDRO versions of the MACSIS clusters were then post-processed with the SUBFIND algorithm (Springel et al., 2001b), a tool developed for identifying locally overdense regions within the FoF objects (Dolag et al., 2009). From a physical perspective, a substructure is defined as a self-gravitating object (analogue to local groups of galaxies) orbiting within the potential well of a larger host cluster. The subhalo detection approach adopted in SUBFIND uses the 3-dimensional position of the particles, smoothed by a locally adaptive kernel, to compute the mass density field. Local maxima in the density will result in subhalo candidates, from which the code will remove the unbound particles with positive total energy. SUBFIND then establishes the edges of the substructure where the density field encounters a saddle point, before reaching the levels of the background halo. Such process defines a self-bound isodensity surface containing the particles bounded to the subhalo. An alternative interpretation of this method involves the detection of local minima in the static gravitational potential, surrounded by an equipotential surface which limits the substructure.

As noted by Springel et al. (2001b) and Onions et al. (2012), SUBFIND only exploits the velocity information for detecting the unbound particles, while the determination of the subhalo candidate relies on the spatial data. Such technique may introduce systematic biases in the subhalo properties, due to the missing kinematic information in the SUBFIND isodensity curves computation, discussed and extended in Behroozi et al. (2013) and Cañas et al. (2019).

SUBFIND can operate on DMO and HYDRO simulations and separates the background ICM, labelled with subgroup number  $n_{SG} = 0$ , from the detected subhalos, to which a progressive  $n_{SG} \geq 1$  is assigned in order of decreasing mass. In the particular case of MACSIS, in order to prevent recursive oversampling, the lower threshold for the definition of a substructure has been set to 20 particles (Dolag et al., 2009) corresponding to  $1.32 \times 10^{11} M_\odot$  and  $2.36 \times 10^{10} M_\odot$  for DMO and gas respectively. In section 3, statistical considerations will contemplate a more conservative threshold of 40 particles.

The output of GADGET-3 and the post processing in SUBFIND consists in a file with `hdf5` extension for each halo, redshift output and DMO/HYDRO version of the zoom simulation, containing information relative to the particles phase-space data and the subgroups. Each file presents a hierarchical structure with attached attributes and 6 main subclasses for each particle type, including gas, high and low-resolution dark matter (DM), stars and black holes. The files were processed using Python 3 codes developed by the project contributors, with the aim of retrieving and analysing the outputs of the MACSIS simulation. An example of the post-processed result for the MACSIS FoF halo 0 is shown in figure 2, where the different colours represent the three dominant particle types, differentiated into subhalo-bound material and FoF halo-bound material. In addition, figure 2 indicates the size of the virial radius  $R_{200}$ , defined by the FoF algorithm as the mean distance from the centre of potential at which the particle density becomes smaller than  $200\rho_c$ , where  $\rho_c$  is the critical density of the Universe (Carlberg et al., 1997). In the processing of the MACSIS zoom simulations the analyses were restricted to the central halo, which by definition (Katz & White, 1993; Tormen et al., 1997; Barnes et al., 2017) is guaranteed to lie within the high-resolution region, bounded by a spherical surface of radius  $5R_{200}$ .

## 3 Matter distribution of substructures

The FoF cluster presented in figure 2 shows an abundance of substructures with a variety of structures, sizes and baryon content. Investigating how such observables correlate with the spatial position and the properties of the local environment surrounding the subhalos is the aim of the present section. In order to draw valid conclusions regarding the subhalos and their

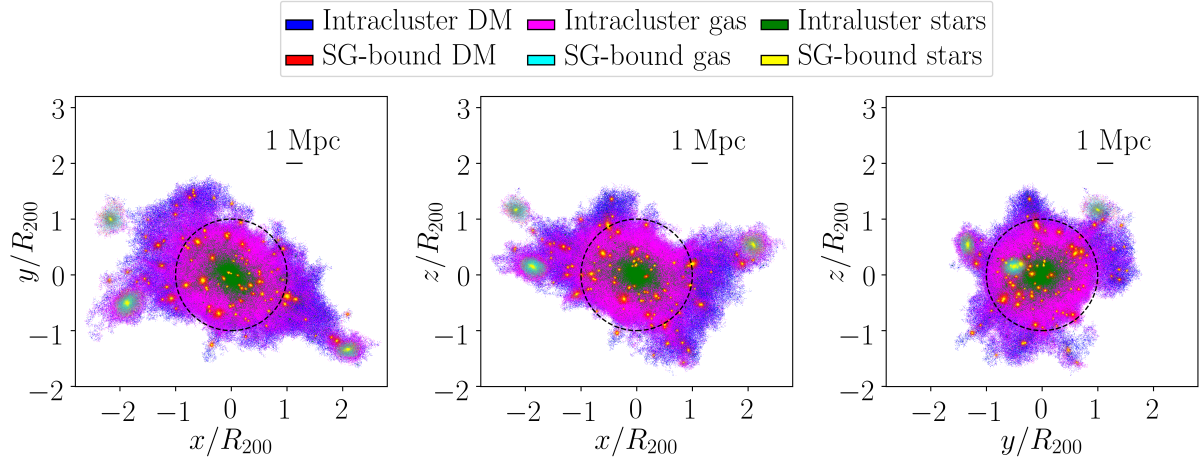


Figure 2: Visualisation of the FoF MACSIS cluster with  $n_{FoF} = 0$ . The object, drawn from the HYDRO simulation, shows the DM, gas and stellar components highlighted with different colours for the background intracluster ( $n_{SG} = 0$ ) and subgroups (SG)-bound particles ( $n_{SG} \geq 1$ ). The plots show the three  $x - y$ ,  $x - z$  and  $y - z$  projections of the FoF cluster, centred on its centre of potential, defined as the global minimum of the potential. The black dashed line marks the size of the virial sphere of radius  $R_{200} = 3.68$  Mpc, with respect to which the axes are scaled. The 1 Mpc length is indicated by the bar in the top-right corner of each plot.

hosts, the density profiles, mass function and mass fractions are examined in detail throughout the following subsections. Such analyses only involved the spatial 3-dimensional information, extended to the whole phase-space description in section 4.

### 3.1 Mass functions

In order to compare the abundances of subhalos with different masses, the mass function (MF) is a widely implemented tool for expressing the number of objects within different mass intervals (Press & Schechter, 1974; Bahcall & Cen, 1993; Dolag et al., 2009). By exporting the SUBFIND outputs and sorting the substructures in order of increasing mass  $M$ , 40 logarithmic mass bins were defined between  $10^{11.5} \leq M/M_\odot \leq 10^{15}$ . After excluding the object orbiting beyond the  $5R_{200}$ -radius sphere in each of the 10 FoF clusters, the total number of subhalos within each mass bin was computed. Such procedure was applied to the DMO version of the simulation, as well as the DM component in the HYDRO simulation. Globally, both versions of the MACSIS run share the same total mass, despite solely being in the form of DM in the DMO case, while presenting several different particle types in the HYDRO realisation. As a consequence, in order to compare the DM content from the two datasets, it is necessary to normalise the total DMO mass with respect to the universal DM fraction  $\overline{f_{DM}}$ , defined as

$$\overline{f_{DM}} = \frac{\Omega_{DM}}{\Omega_m} \equiv 1 - \frac{\Omega_b}{\Omega_m}, \quad (6)$$

where  $\Omega_m$ ,  $\Omega_{DM}$  and  $\Omega_b$  express the cosmological mass, DM and baryon density respectively, as given in Planck Collaboration et al. (2014a,b) and Planck Collaboration et al. (2018).

The normalisation resulted in a reduction of 15.6 % of the effective DMO mass, delivering the MFs presented in figure 3. The image shows that the subhalo MF is monotonically decreasing, within the Poissonian scatter and the mass range above the 40-particle limit. Such feature, commonly observed in cosmological survey data (Press & Schechter, 1974; Bahcall & Cen, 1993; Okabe et al., 2014), is a direct consequence of the hierarchical clustering presented in section 1, which implies a larger abundance of smaller objects, followed by rarer mergers having

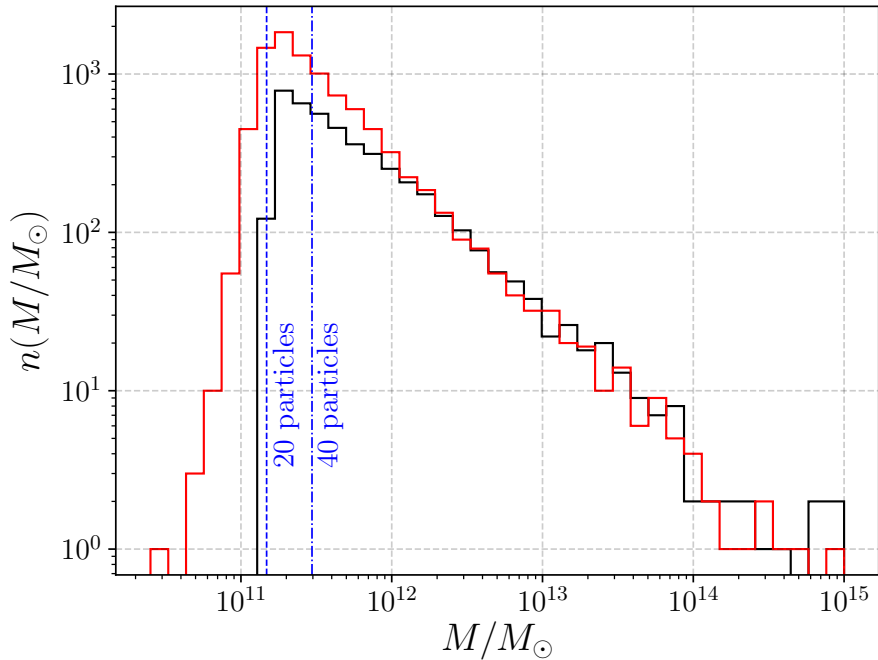


Figure 3: Substructure MFs of the dark matter components for the DMO (black histogram), normalised with respect to  $\overline{f_{DM}}$ , and HYDRO (red histogram) simulations of the 10 largest MACSIS halos. The dashed vertical lines mark the lower mass confidence limits, corresponding to 20 and 40 particles, in compliance with section 2.3.

higher masses (White & Frenk, 1991). Furthermore, the comparison between the two histograms resulted in a close agreement in the large mass regime ( $M \geq 10^{12} M_\odot$ ), which is expected from the dominance of DM gravitational interaction on large structures. However, the MACSIS results show a significant discrepancy in the DM information in the low-mass regime ( $M \leq 10^{12} M_\odot$ ) due to the effects of baryonic physics. In particular, radiative cooling is likely to be one of the main contributors to such an effect, favouring the loss of thermal energy in the gas and the subsequent further collapse of small scale structures. The action of feedback and stellar winds, which could have been responsible for the opposite effect, is not observed in the DM component, as the gas does not interact with DM particles via collisional processes. Radiative cooling leads to collapse of gas clouds and is therefore closely related to star formation phenomena. As a consequence, detecting a large stellar mass in subhalos with  $M \leq 10^{12} M_\odot$  would corroborate the hypothesis for the excess in the number of small objects in the HYDRO DM data. Such prediction has been verified and is discussed in detail in section 3.2, which focuses on the baryon fractions. Statistical significance of this effect is supported by the limited stochastic Poisson scatter in the data, deriving from the combination of 10 FoF groups and the large sample of low-mass substructures ( $n > 100$ ). The discrepancy in figure 3 is present even in proximity of the more conservative 40-particle limit, which excludes numerical resolution and aliasing effects dominating the  $M \leq 10^{11} M_\odot$  region.

The above results for the MACSIS substructure MFs show compliance with previously developed simulations (Moore et al., 1999; Springel et al., 2001b; Nurmi et al., 2006; Dolag et al., 2009), provided that the number of substructures is normalised and the mass ranges matched. In particular, differently from the works by Springel et al. (2001b); Dolag et al. (2009) and McCarthy et al. (2017), the MACSIS sample was selected to deliver the optimal results in the large mass regime, at the expenses of poor numerical simulation in the low mass end. As a consequence, the results presented above are featured by a higher statistical significance within

the substructure mass range  $10^{11.5} \leq M/M_{\odot} \leq 10^{14}$ , compared to  $N$ -body simulations involving smaller galaxy clusters.

In order to extend the results presented above, the stellar MF can be computed from the MACSIS HYDRO dataset, in order to relate it to the observed Luminosity Function (LF) deriving from galaxy cluster surveys (Abell et al., 1989; Edge et al., 1990; Bahcall & Cen, 1993). A more detailed discussion of the MACSIS stellar MF, the LF and their relation to observational results may be included in an upcoming work by the author.

### 3.2 Mass fractions

Large galaxy clusters, such as the MACSIS FoF groups examined in this work, are part of the cosmic web and they are surrounded by filaments and voids. This consideration implies that galaxy clusters are relatively isolated objects where the majority of the mass in the Universe is concentrated (White & Frenk, 1991). The proportions of their matter content are therefore expected to reflect the ones of the Universe, which can be obtained from the Cosmic Microwave Background (Planelles et al., 2013; Planck Collaboration et al., 2018). The study of the matter composition of clusters is therefore a strong test of the  $\Lambda$ CDM model at cosmological scales, as well as a useful indicator of the composition of their smaller subgroups, as shown in this section.

The subhalo MFs provide statistical information about the abundance of objects within a specific mass range, although they do not specify the matter content of the subgroups. Mass *fractions* can be regarded as an extension of MFs, allowing simpler visualisation of the relative abundances of the subhalo masses, together with the baryonic and non-baryonic content. The relevance of mass fractions is strictly related to the study of HYDRO simulations, which involve the gas, stellar, black hole and DM particle types. In analogy with section 3.1, the computation of the mass fractions was based on the results of SUBFIND, sequentially applied to each particle type, with the aim of retrieving the mass of each subhalo associated with the gas, stellar (where the black holes are also included) and DM counterparts. In order to restrict the analysis to the FoF high-resolution region, only the subgroups within  $5R_{200}$  were considered and their total mass  $M$  calculated as  $M = M_{stars} + M_{gas} + M_{DM}$ , where  $M_{stars}$  expresses the mass of the stars identified in the subgroup,  $M_{gas}$  the gas mass and  $M_{DM}$  the one associated with non-baryonic material. The baryonic mass is instead given by  $M_b = M_{stars} + M_{gas}$  and is used to compute the subhalo baryon fraction, defined as  $f_b \equiv M_b/M$ . Similarly, the non-baryonic DM fraction can be written as  $f_{DM} \equiv M_{DM}/M$ , followed by the stellar fraction  $f_{stars} \equiv M_{stars}/M$  and the gas fraction  $f_{gas} \equiv M_{gas}/M$ . Such values were calculated for each subgroup and then binned with respect to  $M$ ,  $f_{stars}$ ,  $f_{gas}$ ,  $f_b$  and  $f_{DM}$ , with each bin expressing the number of subhalos within a specified mass and fraction range. The results, shown in figure 4, are visualised as density plots, for which the median, the 16<sup>th</sup> and 84<sup>th</sup> percentiles have also been calculated within logarithmically spaced mass bins. Moreover,  $f_b$  and  $f_{DM}$  have been normalised to the universal baryon fraction  $\overline{f}_b$  and the universal DM fraction  $\overline{f}_{DM}$  respectively, where

$$\overline{f}_b = \frac{\Omega_b}{\Omega_m} = 0.1564 \pm 0.0016 \quad \text{and} \quad \overline{f}_{DM} = \frac{\Omega_{DM}}{\Omega_m} \equiv 1 - \overline{f}_b = 0.8436 \pm 0.0016, \quad (7, 8)$$

were obtained by Planck Collaboration et al. (2014b,a, 2018) and following equation 6. In equations 7 and 8,  $\Omega_m$  indicates the total matter density of the Universe,  $\Omega_b$  indicates the baryon density and  $\Omega_{DM}$  the DM density, as derived from Cosmic Microwave Background (CMB) observations. The mass fractions for the considered MACSIS subhalos show a considerable scatter in the low-mass range ( $M \leq 10^{13} M_{\odot}$ ), in addition to a significant discrepancy from the values of  $\overline{f}_b$  and  $\overline{f}_{DM}$  resulting from CMB experiments, as observed in figures 4 (C) and (D). Such scatter indicates that the substructures do not exhibit a uniform abundance of stars, gas and DM: they are subject to thermodynamic and gravitational interactions with the host cluster, which plays a role in processes of accretion and stripping of material. Such dynamics

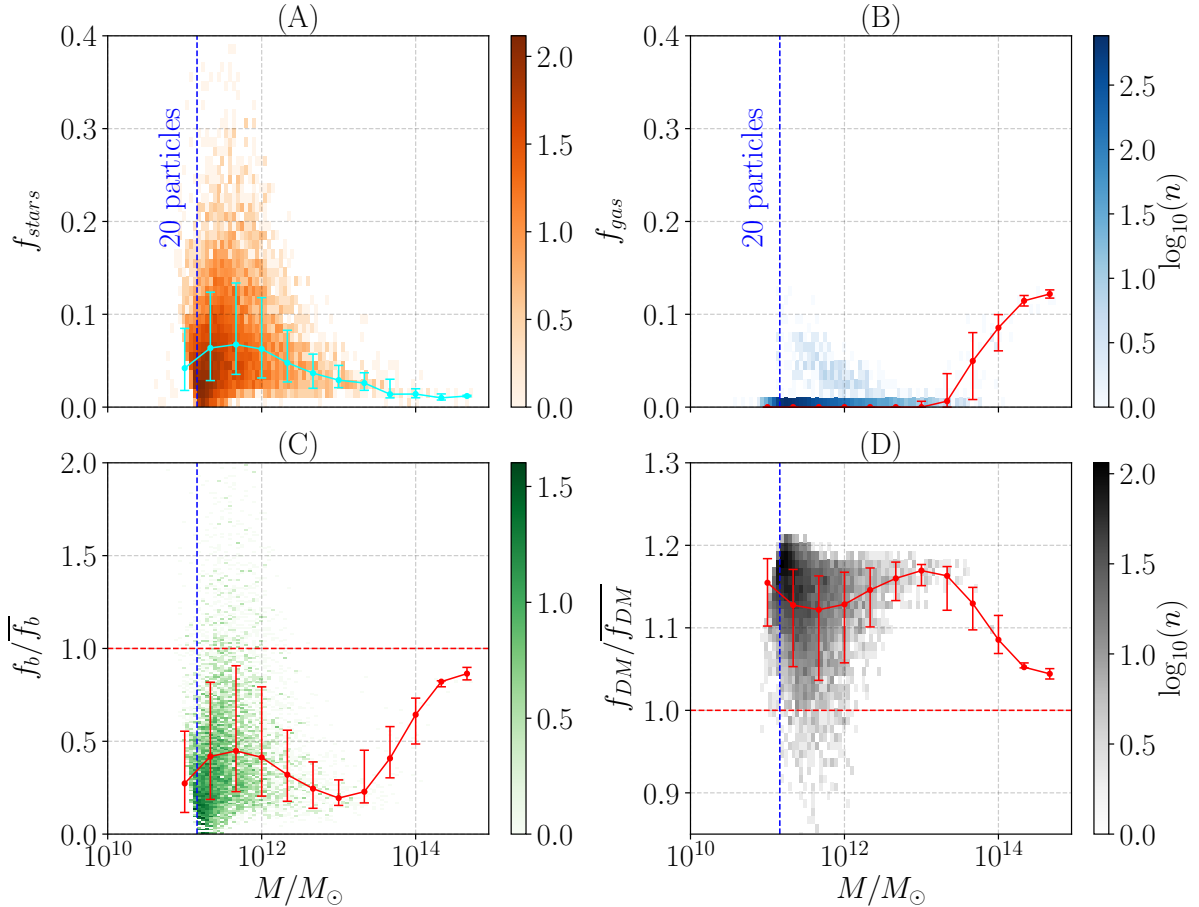


Figure 4: Mass fractions for the subgroups within  $5R_{200}$  populating the MACSIS clusters with  $n_{FOF} \leq 10$ . The figure reports the stellar mass fraction (A), the gas mass fraction (B), the baryon fraction (C) and ultimately the DM fraction (D), as a function of the total mass of the subhalos. Each of the 4 density plots are presented with a colour bar specifying the logarithm of the number  $n$  of subgroups counted in each bin. In addition, the lines and bars superimposed to the density plots indicate the median value of the fractions at equally spaced mass bins, as well as the corresponding 16<sup>th</sup> and 84<sup>th</sup> percentile levels. The dashed red lines in plots C and D highlight the values for the universal baryon and DM fractions, while the dashed blue lines mark the 20-particle confidence limit, motivated in section 2.3.

heavily affects the composition of substructures, leading to the large scatter highlighted by the significant percentile bars in figure 4. Substructures cannot therefore be regarded as isolated systems, since they continuously exchange material with the surrounding ICM, the host DM halo and also with other substructures in the case of mergers. Conversely, the CMB is often regarded as an isolated system within experimental uncertainties, while large galaxy clusters can be approximated as isolated systems, after neglecting the accretion of material from the filaments of the cosmic web. Such nature renders them much more accurate indicators of the baryon and matter fractions on cosmological scales, since they contain a larger mass sample, statistically affected by a smaller scatter (Planelles et al., 2013). As a direct consequence of such consideration, the MACSIS subhalo mass fractions are expected to display a decreasing scatter at progressively higher values of  $M$ , together with median values approaching the universal baryon and DM fractions.

Focusing on the stellar mass fraction, illustrated in figure 4 (A), it is possible to observe an abundance of substructures with  $M \leq 10^{13} M_\odot$  which are relatively rich in stars, likely due to the fact that most objects within the same mass range lack of gas, with the result of increasing

the relative proportion of  $f_{stars}$ . The median profile followed by the stellar mass function is also a consequence of the star formation mechanisms implemented in GADGET-3 and discussed in Schaye & Dalla Vecchia (2008) and McCarthy et al. (2017), which depends on the assumption of an initial mass function and free parameters tuning.

The gas fraction (figure 4 B) shows instead a scarcity of material for small subhalos, highlighted by the negligible percentile bars around  $f_{gas} = 0$  for  $M \leq 10^{13} M_\odot$ . Two major contributions have been advanced in order to explain this effect. Firstly, the majority of such population of substructures in fact lies within  $R_{200}$ , hence immersed in the ICM of the FoF halo. In the process of orbiting the system and entering the host cluster's medium for the first time, their gas has been shocked and stripped due to ram pressure, leaving the denser stellar core exposed to the FoF environment, as well as the non-interacting collisionless DM. Such effect has been extensively observed at the scales of galactic halos within larger galaxy groups (Balsara et al., 1994; Abadi et al., 1999; Vollmer et al., 2001) and is here proved to contribute to the composition of subgroups within larger halos. The second effect leading to a lack of gas is star formation itself: the substructure potential well due to baryons and DM, in addition to radiative cooling mechanisms, triggers the collapse of gas clouds and the conversion of gas into stellar cores. Such phenomena are modelled by the subgrid physics discussed in section 2 and are not individually identified at the particle resolution typical of MACSIS. The very low  $f_{gas}$  exhibits a significant rise up to  $0.122 \pm 0.004$  starting from  $10^{13} M_\odot$ , as deduced by rarer more massive subhalos lying beyond  $R_{200}$ , but still within the  $5R_{200}$  high-resolution volume. Such objects have not experienced ram pressure stripping, since they gravitate outside the high-density ICM; they are also featured by a higher mass tracing a deeper potential well than small objects, causing a higher fraction of the gas to be bound to the system.

The discussion of the  $f_{stars}$  and  $f_{gas}$  profiles is necessary to interpret the overall shape of  $f_b/\bar{f}_b$  plot, exhibiting a local maximum in the lower mass regime due to stellar components, followed by the gas-dominated high mass range, causing it to approach the  $f_b/\bar{f}_b = 1$  line, as shown by figure 4 (C). The presence of subhalos with  $f_b > \bar{f}_b$  is justified by processes of accretion, due to the infall of baryons induced by the gravitational potential well. Ultimately, the shape of DM fractions in MACSIS HYDRO simulation suggests a  $f_{DM} > \bar{f}_{DM}$  for the majority of subhalos within the 10 most massive FoF groups. This effect is partly due to collisionless nature of DM, which protects DM subhalos from ram stripping and related collisional thermodynamic processes, but mostly related to the definition of  $f_{DM}/\bar{f}_{DM}$  ratio in equation 8. The complementarity relation between baryon and DM fractions can therefore explain the correlations in the profiles of  $f_b$  and  $f_{DM}$ , where the scatter can be geometrically mapped by a translation and reflection about the  $f_{DM}/\bar{f}_{DM} = 1$  level. The physical interpretation of such property indicates that numerous substructures show a high DM fraction, caused by their baryonic content being stripped and therefore resulting in a higher *relative* DM fraction. Additionally, the plot in 4 (D) may also include information about subhalos whose DM structure has been disrupted by tidal forces due to the host cluster gravitational field or by high velocity encounters with other substructures. The study of such effects would require analyses of merger trees (Wechsler et al., 2002; Tweed et al., 2009), which are not included within the present work.

### 3.3 Density profiles

The structure of galaxy clusters is defined by the spatial mass distribution of the different components constituting the object. In order to probe such structure, density profiles are commonly used in the field of Astrophysics research to study the mass content of an object at different radii from its centre. They are a direct consequence of the  $\Lambda$ CDM model, as they can be related to the CMB power spectrum and the value of the cosmological parameters. The quest for a universal model for density profiles arose simultaneously with the development of high-resolution  $N$ -body simulations, leading to the work by Navarro et al. (1997), which introduced

the *NFW profile*. Such analytical model is currently the most widely accepted framework for the analysis of DM halos, since it proved to be capable of describing numerous structures in the context of hierarchical clustering, as shown by recent observational results (Prat et al., 2018). Mathematically, the NFW profile relates the mean density  $\rho(r)$  of a DM halo at a radius  $r$  from its centre, as expressed by

$$\rho(r) = \frac{\delta_c}{\frac{r}{R_s} \left( \frac{r}{R_s} + 1 \right)^2}, \quad (9)$$

where  $\delta_c$  is the characteristic density parameter and  $R_s$  the scale radius of the halo. In order to compare the NFW profile for different DM groups, it is common practice to normalise  $r$  to the virial radius  $R_{200}$  and  $\rho(r)$  to the critical density of the Universe  $\rho_c$ , following the definitions in section 2.3. In addition, Navarro et al. (1997) introduced the dimensionless quantity  $c \equiv R_{200}/R_s$ , known as the concentration of the halo, which indicates ratio between the size of the central region of the cluster and its virial radius.

The computation of the density profile of an object involves the identification of its centre of potential and the subdivision of the surrounding space by concentric spherical surfaces with logarithmically increasing radial bins. The mass content, obtained by counting the number of particles in each shell and correcting for appropriate mass units, is then divided by the volume of the shell, in order to deliver  $\rho(r)$ . This procedure was applied to the 10 MACSIS FoF groups in object, rescaling  $\rho(r)/\rho_c$  and  $r/R_{200}$ . The result, consisting in 10 density profile datasets, was combined by calculating the median value of  $\rho(r)/\rho_c$  at each radial bin, alongside with the 16<sup>th</sup> and 84<sup>th</sup> percentile levels indicating the scatter in the samples. Figure 5 displays the outcome of such analysis extended to the 10 largest MACSIS mergers, in the case of DM halos drawn from the DMO simulation and those populating the HYDRO run, after applying an appropriate mass normalisation, in analogy with the MFs in section 3.1.

The median of the density profiles deriving from all the FoF-bound DM particles was fitted using the NFW model presented by equation 9. The upper limit in  $r$  was set to  $R_{200}$ , since the region within the virial sphere of a cluster contains by definition the self-bound material, in agreement with the NFW model being formulated for gravitationally self-bound DM halos. The necessity of a lower limit for the fit arises mathematically from the singularity in equation 9 at  $r = 0$ , which predicts a diverging DM density at the centre of the cluster. Although the NFW profile suffers from such field discontinuity, *N*-body simulations are generally not affected by this unrealistic inconsistency: firstly, the introduction of the Plummer softening scale, discussed in section 2.1, would impede any significant study at  $r < \epsilon = 4 h^{-1}\text{kpc}$  (MACSIS zoom-simulation) due to the softened Newtonian potential; secondly, the finite particle resolution would further mitigate the steep NFW profile due to lack of samples within the very central regions of galaxy clusters. The latter effect, known as *numerical convergence* problem, causes the DM density profiles to flatten at small radial distances, resulting in an underestimate of  $\rho(r)$ . Power et al. (2003) extensively studied such numerical resolution effect by comparing simulations with different  $\epsilon$ -softening and different particle resolutions, leading to the definition of the convergence radius  $R_{conv}$ . According to Fukushige & Makino (2001), the innermost radius within simulated galaxy clusters that can be resolved is featured by the 2-body relaxation time  $t_{relax}$  of the order of the Hubble time  $t_0$ . Such definition has been further developed by Power et al. (2003), leading to the numerical convergence condition

$$\alpha(r) \equiv \frac{t_{relax}(r)}{t_0} = \frac{\sqrt{200}}{8} \frac{N(< r)}{\ln N(< r)} \left( \frac{\rho(r)}{\rho_c} \right)^{-\frac{1}{2}} \sim 1, \quad (10)$$

where  $\alpha(r)$  is the relaxation coefficient and  $N(< r)$  is the number of particles orbiting at distances less than  $r$ . For the MACSIS FoF clusters,  $R_{conv}$  has been computed by passing the  $\alpha(r)$  values to the `scipy.optimize.fsolve` function, in order to find the radius at which it

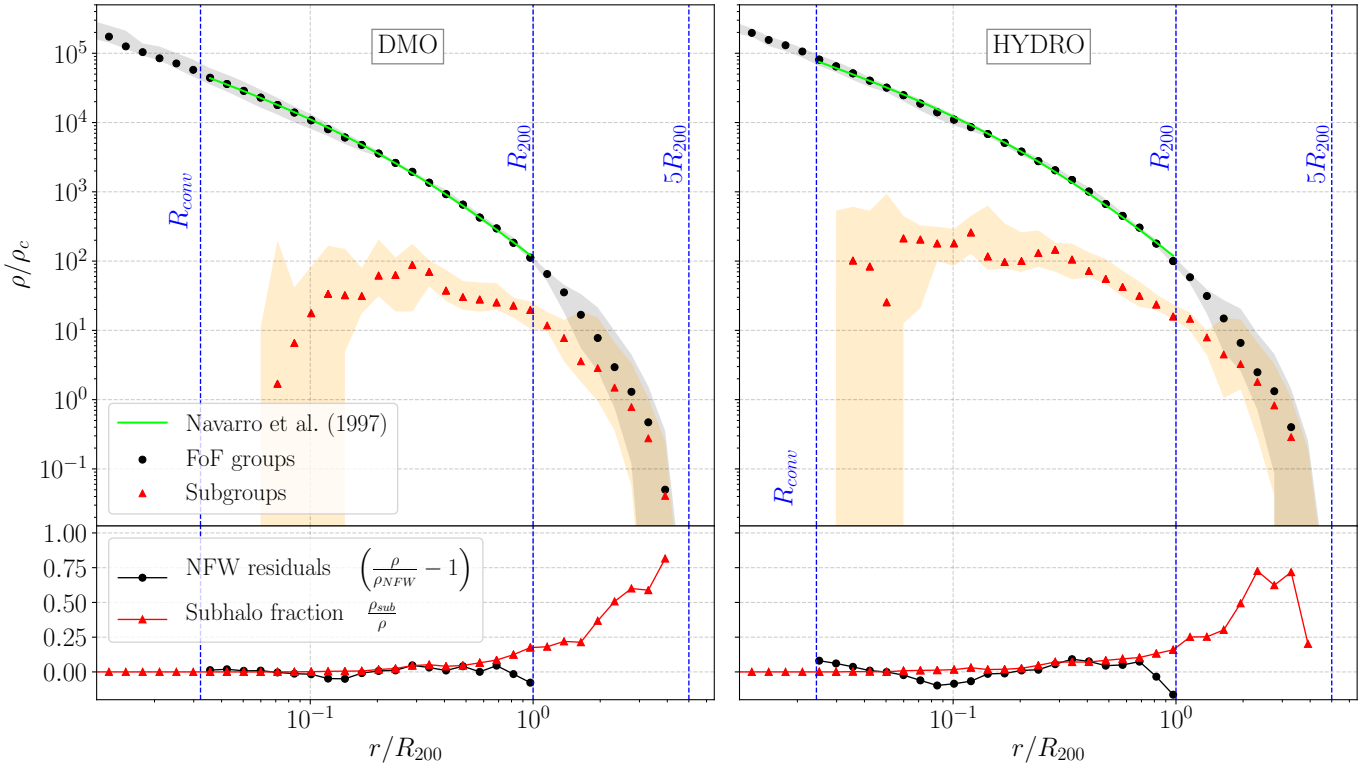


Figure 5: Combined density profile for the 10 largest MACSIS FoF groups from the DMO (left panel) and the HYDRO (right panel) simulations. The black filled circles mark the density profile calculated using all the FoF high-resolution DM particles, while the red triangles represent the density profile of the subhalo-bounded particles only. Both plots extend out to  $5R_{200}$ , with vertical dashed blue lines indicating the high-resolution simulation boundary, in addition to  $R_{200}$  and the convergence radius  $R_{conv}$  (Power et al., 2003). The grey and orange shaded regions represent the 16<sup>th</sup> and 84<sup>th</sup> percentile levels, based on the scatter of the data derived from mediating the 10 clusters. The green line fits the FoF density profiles according to the NFW model (Navarro et al., 1997), which resulted in the fractional residuals displayed by the black filled circles in the lower plots. Ultimately, the red triangles in the bottom plots express the ratio between the subhalo and the FoF profiles, quantifying the subhalo fraction.

equals unity. This procedure was applied to each FoF cluster from the DMO and HYDRO data. The applied NFW inner limit was conservatively chosen to be the largest convergence radius in each dataset, which resulted in  $R_{conv} = 0.032 R_{200}$  for the DMO simulation and  $R_{conv} = 0.024 R_{200}$  for the HYDRO DM component.

The optimal fit parameters minimising the  $\chi^2_{reduced}$  based on the percentile scatter are summarised in table 1. As suggested by figure 5 and the NFW parameters, no considerable difference in the density parameter is noted between the DMO and HYDRO datasets. However, the median sample concentration was found to be higher in the HYDRO case than in the DMO halos, confirming the results obtained by Henson et al. (2017). Furthermore, such discrepancy can be explained by analogous arguments to section 3.1: baryons introduce dissipative processes, such as radiative cooling, which results in a loss of energy and further contraction of the medium. The reliability of the NFW fit is also proved by the dimensionless fractional residuals, shown in the lower panels in figure 5, where they are expressed as  $(\rho - \rho_{NFW})/\rho_{NFW}$ . Minor fluctuations in the residuals, with amplitude smaller than 0.1, can be identified in correspondence of large number of substructures, where the overdensity produces a  $\rho(r)$  higher than the theoretical NFW profile.

Ultimately, the NFW model predicts the density profile of DM halos to fall proportionally

Table 1: Table showing the optimal NFW fit parameters relative to the 10 largest MACSIS FoF clusters. The errors, deriving from statistical scatter in the data, were obtained from the diagonal terms in the `scipy.optimize.fsolve` covariance matrix. The fitting procedure, extended to DMO and HYDRO simulations, was based on the evaluation of the convergence radius, which is also reported below. The angle brackets indicate the median value of the DM halo concentration  $\langle c \rangle$  for the cluster sample examined, having total masses  $M_{FoF} \gtrsim 10^{15.8} M_\odot$  (Barnes et al., 2017).

	DMO	HYDRO
$\log_{10}(\delta_c/\rho_c)$	$3.77 \pm 0.03$	$3.89 \pm 0.06$
$R_s/\text{Mpc}$	$0.330 \pm 0.006$	$0.295 \pm 0.009$
$\langle c \rangle$	$4.93 \pm 0.09$	$5.51 \pm 0.18$
$\max(R_{\text{conv}}/R_{200})$	0.032	0.024

to  $r^{-1}$  for small radii and to  $r^{-2}$  at large radii. Despite delivering a reliable representation of the results within radii  $[R_{\text{conv}}; R_{200}]$ , it fails to accurately reproduce the density behaviour outside this range. In particular, for  $0 < r \leq R_{\text{conv}}$  the profile falls less rapidly than  $r^{-1}$  due to numerical convergence effects, while for  $r \geq R_{200}$  the profile decay is steeper than  $r^{-2}$ , as observed in figure 5. This effect has been studied in order to study the *backsplash* radius and the population of substructures and galaxies gravitating within it (Gill et al., 2005).

Lastly, in order to compare the total FoF distribution of particles with that restricted to substructures only, additional density profiles have been obtained by selecting the DM particles bound to the subhalos. The results, shown in the same plot as the FoF profiles (figure 5), are followed by the calculation of the subhalo density fraction  $\rho_{\text{sub}}/\rho$ , which indicates the ratio between the subhalo-only profile and the FoF profile. The DMO data revealed that the particles constituting substructures show a maximum in the density around  $r = 0.2 R_{200}$ , before decaying at inner radii  $r \lesssim R_{\text{conv}}$ . The effect of such cut-off may be due to three effects: firstly, substructure-bound particles within a small region close to the centre of the galaxy cluster are statistically rare, since the volume of the sampling domain is three orders of magnitude smaller than  $R_{200}^3$ . Secondly, DM structures in the vicinity of the centre of the FoF group are subject to intense tidal forces, which may prevent substructures from coalescing and forming a stable self-gravitating population. Thirdly, the SUBFIND algorithm for the detection of overdensity regions may not be robust enough to identify candidates in regions with very steep density fields. More recent developments (Onions et al., 2012; Behroozi et al., 2013; Cañas et al., 2019) improved the capabilities of substructure detection codes, including velocity information and mitigating the SUBFIND systematic bias. Despite the presence of biases, the comparison between the substructure density profile in the DMO and HYDRO simulations can be used to draw valid conclusions, since both datasets are affected by the same systematics. In particular, the MACSIS HYDRO substructures show a higher particle density at radii approaching  $R_{\text{conv}}$  than in the DMO case. Following section 3.1, the decrease in the DMO density  $\rho_{\text{sub}}(R_{\text{conv}} < r < 0.2 R_{200})$  can also be interpreted by a decreased abundance of substructures close to the FoF centre of potential due to absence of dissipative astrophysical processes. Conversely, radiative cooling favours the formation of subhalos within the central FoF regions, resulting in higher DM substructure density, more compact objects and a higher resistance to tidal disruption. This result confirms the MF discrepancy found between DMO and HYDRO subhalos, providing additional spatial information and suggesting the presence of smaller and compact substructures close to the FoF centre of potential.

The subhalo density fraction, displayed in figure 5, shows a negligible substructure contribution to the overall FoF density at low radii, with values increasing to 19% at  $r = R_{200}$  and up to 78 % (DMO) and 74 % (HYDRO) closer to  $r = 5R_{200}$ . The substructure content is hence dominant outside the FoF virial sphere, with the presence of larger self-bound object,

whose growth is favoured by a lower gravitational influence from the main cluster. Analyses of such subhalo population would require more extended zoomed simulations and higher particle resolution, which would respectively result in more accurate data beyond  $r = 5R_{200}$  and smaller statistical scatter in the percentile levels, responsible for the anomalous values of  $\rho_{sub}/\rho$  at  $r \simeq 5R_{200}$ .

## 4 Kinematic properties

As preluded in the introduction to section 3, the description of galaxy cluster subhalos would be incomplete without detailed analysis of the whole 6-dimensional phase-space. The present section is aimed at extending the overview of the distribution of substructures by studying their kinematic properties, in relation to the positional information. In the context of galaxy clusters, the velocity domain owes its importance to its link to observables, in particular the possibility of measuring the line-of-sight velocity of objects from their doppler signature. Such analysis is key for performing estimates of the dynamical mass of galaxy clusters (Zwicky, 1933), in addition to hints on the dynamical evolution of systems of complex mergers, such as the clusters subjects of this work. In particular, cosmological simulations are a crucial tool in the advancement of the field of galaxy cluster Astrophysics, since they can produce the 3-dimensional velocity vectors of the material within the system, while the only accessible observable consists in the radial component. Evidence for substructures in galaxy clusters can therefore be evinced from line-of-sight velocity data (Fitchett & Webster, 1987; Dressler & Shectman, 1988), while simulations can shed light upon the inaccessible tangential velocity components (De Boni et al., 2018), enhancing the accuracy of mass estimates and the characterisation of potential physical biases.

The processing pipeline for velocity information was based on the extraction of data from **hdf5** files, similarly to the previous cases, resulting in the three Cartesian components  $v_x$ ,  $v_y$  and  $v_z$ , relative to each particle in the system. The velocity components were then normalised to the zero-momentum frame of the FoF cluster, which shows a bulk motion induced by tidal forces and interactions with large scale structures and the cosmic web. The centre-of-mass frame was defined by the velocity vector resulting from averaging all the FoF particles, for which the radial distance from the centre of potential was also computed, following the methodology of section 3. The plot of the velocity components of each particle against its radial distance are known as velocity distributions and they constitute a crucial tool for performing a kinematic analysis of the galaxy cluster. In analogy with previous sections, the particles bound to the host FoF halo and those unbound were filtered out, retaining only the particles bound to the substructures orbiting within  $5R_{200}$ . The radial distance data and the velocities were then binned according to linear scales and the result of such procedure can be visualised as a density plot, whose colour gradient is a measure of the number  $N$  of particles. Figure 6 illustrates the velocity distributions for the DMO simulation and the HYDRO (DM and stars) dataset, relative for largest MACSIS FoF cluster ( $n_{FoF} = 0$ ) and for  $r \leq 5R_{200}$ .

The line-of-sight velocity in the cluster rest-frame was conventionally chosen to be  $v_z$  and is reported due to its significance in galaxy clusters redshift surveys (Davis & Peebles, 1983; Colless et al., 2001). The physical velocity  $|\mathbf{v}| \equiv \sqrt{v_x^2 + v_y^2 + v_z^2}$  shows particles being distributed in the lower region of the plots bounded by an envelope. Such boundary marks the value of the escape velocity of substructures orbiting the main halo, for which the total classical energy vanishes. As expected from the discussion on the SUBFIND code, no particle is expected to lie above the escape velocity boundary: this condition would involve a positive total energy, resulting in the object to be unbound to the cluster and by definition rejected by the algorithm. The profile of the envelope can be derived from the NFW model of a spherically symmetric DM halo and fitted to the dataset, in order to infer the mass of the cluster. Such technique, known

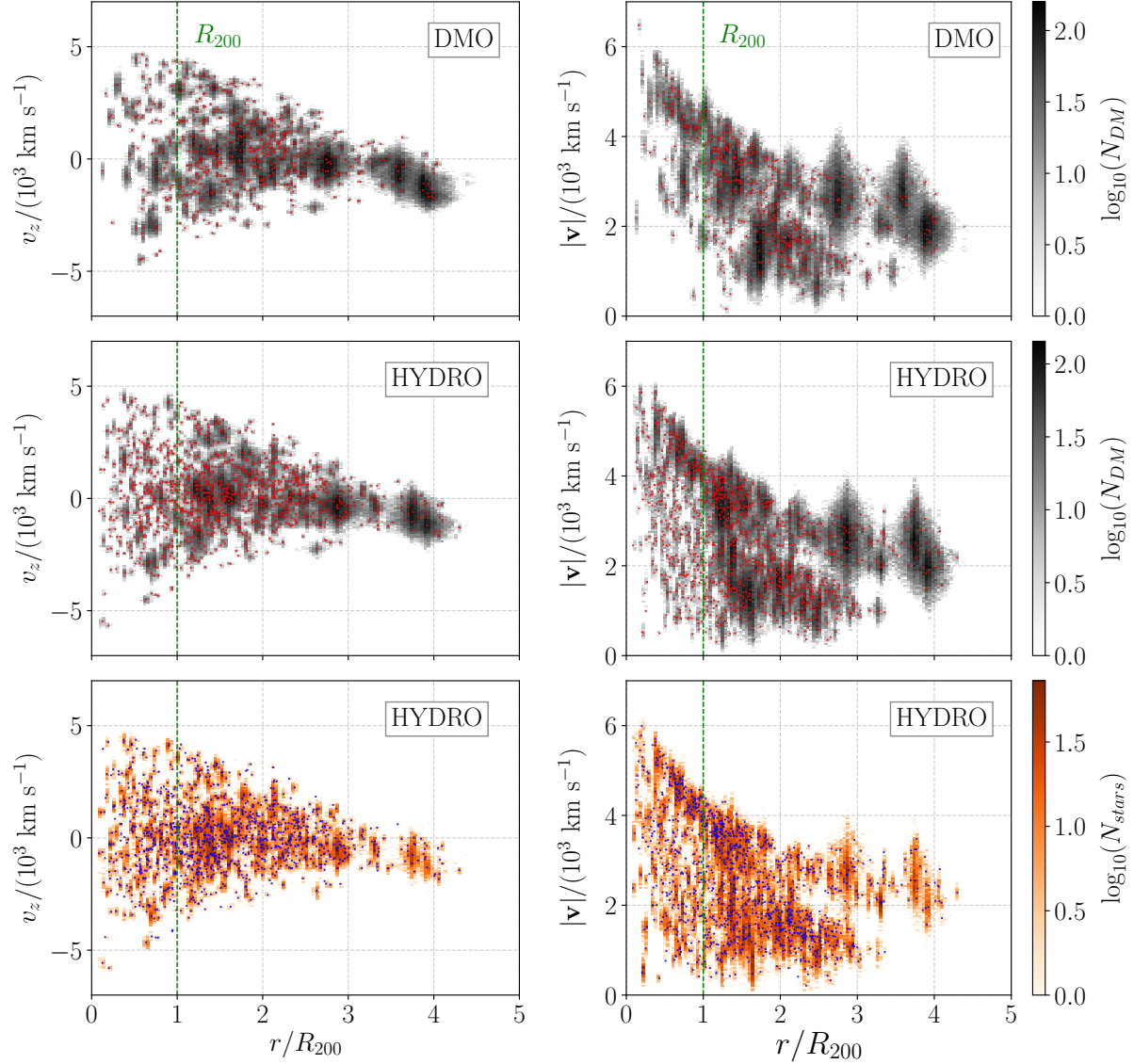


Figure 6: Velocity space distributions for the subhalo-bounded particles (density plots) belonging to the MACSIS FoF cluster with  $n_{FoF} = 0$ . The superimposed red (DM) and blue (stars) markers indicate the position and velocity averages of all substructures within the high-resolution region. The results reported in this figure show an example of line-of-sight velocity ( $v_z$ ) and the magnitude of the velocity vector  $|\mathbf{v}|$ . For comparison purposes, the DM particles are displayed for the DMO simulation (top two panels) and the HYDRO sun (middle two panels), while the stars only appear in the HYDRO dataset (bottom two panels). The number of particles in each plot is expressed as  $N_{DM}$  and  $N_{stars}$  for the DM and star particles respectively. Since plots in each row represent the same dataset, they were produced from the same number of particles, hence leading to the same colorbar, which is drawn only once for each case. Lastly, the green dashed line marks the position of the virial radius in each plot.

as caustic method (Gifford et al., 2013), presents several difficulties in the case where only  $v_z$  can be measured, or in the case of highly asymmetric DM distributions. Examining the results in figure 6, it is possible to note significant anomalies in the velocity distribution of the DM and star particles for  $1 < r/R_{200} < 5$ , which do not reflect the canonical shape of the NFW escape velocity envelope. In fact, objects within this regions are not gravitationally dominated by the central cluster and they may form self-bound structures, which interact with the main halo in merging processes.

The importance of the subhalo velocity distributions is also due to the spatial and velocity-domain information that can be inferred from the same plot. Particles bound to subhalos appear as denser regions, whose horizontal elongation expresses their physical size, while their vertical elongation indicates their velocity dispersion. The average of both radial extension and velocity dispersion for each substructure is represented by red (DM) and blue (stars) markers in figure 6. Finally, the position of the markers, indicating the bulk motion of substructures, can be compared in the DMO and HYDRO plots, revealing the stars to be reliable tracers of the HYDRO DM. Moreover, the minor offset in the position and kinematic behaviour of substructures in the DMO and HYDRO DM can be attributed to the gravitational effects of baryons, subject to collisional and dissipative processes.

The study of the bulk velocity of substructures in galaxy clusters will be of paramount importance in the velocity-dispersion relation and in the characterisation of the kinetic Sunyaev-Zel'dovich (kSZ) signal, caused by inverse Compton scattering of CMB photons transiting the ICM of the host halos, as well as the locally overdense subgroups. Further details of such technique for the investigation of the properties of galaxy clusters and their relation to observational findings will be presented in the second part of the project.

## 5 Summary and future work

Hydrodynamical  $N$ -body simulations were used to study the spatial and kinetic properties of substructures populating the 10 largest FoF objects modelled within the MACSIS project. The galaxy clusters involved in the present work were the result of a processing pipeline, consisting in the implementation of gravity, hydrodynamical and subgrid physics routines in the Lagrangian TreePM-SPH GADGET-3 code (Springel, 2005; McCarthy et al., 2017), in order to produce simulated data to be analysed with the FoF and SUBFIND algorithms (Davis et al., 1985; Springel et al., 2001b). The identified substructures were then analysed in the case of the gravity-only (DMO) simulation and the version including hydrodynamics and baryonic physics (HYDRO). A visual inspection of the morphology of the FoF clusters revealed a complex structure, resulting from multiple merging events with neighbouring objects. Such scenario is predicted by the  $\Lambda$ CDM model and reproduced by several hierarchical structure formation studies of large ( $M_{FoF} \sim 10^{15.8} M_\odot$ ) galaxy clusters. Such environment is therefore ideal for the analysis of substructures, whose abundance and mass spectrum were probed using mass functions (MF). The HYDRO MF revealed a significantly larger number of substructures with lower masses than in the DMO run. Such effect was attributed to the baryonic contribution of dissipative processes, which favour the coalescence and further growth of small subhalos with masses  $M_{sub} < 10^{12} M_\odot$ .

In order to validate the conclusions drawn from the MFs and extend them, the study of mass fractions was performed on the HYDRO simulation, highlighting an absence of gas particles bound to subhalos with  $M_{sub} < 10^{13} M_\odot$ . Two main causes have been identified in order to explain such peculiarity: firstly, the subhalos entering the ICM region for the first time lost their gas component due to ram pressure, exposing the denser stellar and DM cores; secondly, star formation processes require the collapse of gas clouds in order to be initiated, with the subsequent reduction of gas mass and incremented stellar mass. The overall baryonic components give rise to a baryon fraction that approaches the cosmological CMB value at large

masses ( $M_{sub} > 10^{14} M_{\odot}$ ), as expected from statistical considerations of large mass and volume samples. Large scatter above the universal value in the baryon fraction was attributed to accretion of baryons due to hydrodynamical subhalo interactions and their deeper potential wells, while the relative DM fraction significantly above the universal value was explained both in mathematical terms and with the lower abundance of baryons in most substructures.

The study of the distribution of substructures is concluded with the interpretation of DM density profiles for both the DMO and HYDRO simulations. The median density profile for the 10 most massive MACSIS FoF groups was computed and an NFW model was fitted between the limits of the numerical convergence radius (Power et al., 2003) and the virial radius. The best fit parameters indicated a larger median concentration in the HYDRO clusters than in the DMO case, in agreement with Henson et al. (2017). The calculation of the density profiles was then repeated for the subhalo-bound DM particles only, revealing significant differences in their distribution. The DMO subhalo profile was featured by a cut-off radius, motivated by statistical likelihood of observing less subhalos within a small volume around the centre of potential, tidal disruption and SUBFIND biases in presence of steep density fields. Since both DMO and HYDRO datasets were analysed using the same routines, both results were expected to be affected by the same degree of bias, allowing a comparison between them. Unlike the DMO subhalo density profile, the HYDRO DM objects showed a higher particle density in the central region, supporting the calculation of the higher average concentration of the clusters and corroborating the hypothesis related to the baryonic effects in the subhalo MFs.

The results section ultimately includes a kinematic study of the galaxy cluster substructures, presenting plots for the subhalo line-of-sight velocity and the physical velocity, which were used to compute the velocity corresponding to the bulk motion of substructures. Such result will be extensively used in an upcoming treatment of the kSZ effect.

## Future work

The investigation of the matter distribution of substructures and their kinematic behaviour could be extended to the relaxed, less massive MACSIS FoF halos, in order to highlight potential variation in the properties of subgroups related to merging processes. The constraint to the analysis of the clusters at present redshift may also be released, revealing the time evolution of MFs, mass fractions, density profiles and velocity distributions. Such study would benefit from the use of merger trees, in order to reconstruct the interaction history of substructures and their role in the formation of large galaxy clusters via hierarchical structure interactions.

The relevance of the  $z > 0$  MACSIS data is also correlated to modelling observations of distant galaxy clusters in the Universe, in order to reconstruct line-of-sight velocity maps (Davis & Peebles, 1983; Colless et al., 2001), gravitational lensing effects Henson et al. (2017) or especially Sunyaev-Zel'dovich signals (Allen et al., 2011; Mayet et al., 2017; Di Mascolo et al., 2018; Lopes et al., 2018; Adam et al., 2018). The next part of the project will extensively involve the calculation of kinetic Sunyaev-Zel'dovich maps for the MACSIS HYDRO clusters, with particular interest in the substructures, their contribution to the CMB spectrum and their role in the study of the host halo(Sayers et al., 2013). The line-of-sight velocity and the bulk motion of substructures, illustrated by the left panels and markers in figure 6, will be crucial in the characterisation of the kSZ effect for subhalos populating large clusters.

The work will then focus on the comparison with recent observational kSZ data from the high-resolution Néel IRAM KID Array (NIKA) camera (Monfardini et al., 2010), resulting in a more comprehensive subhalo study of large galaxy clusters in the process of merging, such as MACS J0717.5+3745 (Adam et al., 2017; Jauzac et al., 2018).

## Acknowledgements and contributions

The MACSIS project was carried out using the DiRAC system in partnership with the Virgo Consortium and the Institute of Computational Cosmology at Durham University. The present work summarises and presents the results of the first part of a MPhys Project, in progress at the University of Manchester - Jodrell Bank Center for Astrophysics. The different sections are the outcome of a joint effort among the project supervisor, collaborator and the author, whose detailed contributions are described below.

The author of this work created the **Python-3** framework for the visualisation of FoF halos and substructures, together with the other density plots, while the collaborator contributed in the optimisation of the colour contrast among different components (see figure 2). The construction of MFs resulted from an equal effort from both project contributors, while the baryonic bias was studied in collaboration with the supervisor. The mass fractions and FoF/subgroups density profiles mostly result from the author's work, while the NFW fitting in figure 5 and the subhalo markers in figure 6 have been largely implemented by the project collaborator.

## References

- Aarseth S. J., 1963, *MNRAS*, **126**, 223  
 Aarseth S. J., 1966, *MNRAS*, **132**, 35  
 Aarseth S. J., 1969, *MNRAS*, **144**, 537  
 Aarseth S. J., Hoyle F., 1964, *Astrophysica Norvegica*, **9**, 313  
 Aarseth S. J., Gott J. R. I., Turner E. L., 1979, *Astrophysical Journal*, **228**, 664  
 Abadi M. G., Moore B., Bower R. G., 1999, *MNRAS*, **308**, 947  
 Abell G. O., Corwin Harold G. J., Olowin R. P., 1989, *The Astrophysical Journal Supplement Series*, **70**, 1  
 Adam R., et al., 2017, *Astronomy and Astrophysics*, **598**, A115  
 Adam R., et al., 2018, *Astronomy and Astrophysics*, **614**, A118  
 Allen S. W., Evrard A. E., Mantz A. B., 2011, *Annual Review of Astronomy and Astrophysics*, **49**, 409  
 Appel A. W., 1985, *SIAM Journal on Scientific and Statistical Computing*, **6**, 85  
 Aragon-Calvo M. A., Szalay A. S., 2013, *MNRAS*, **428**, 3409  
 Bahcall N. A., Cen R., 1993, *Astrophysical Journal*, **407**, L49  
 Balsara D., Livio M., O'Dea C. P., 1994, *Astrophysical Journal*, **437**, 83  
 Barnes J., Hut P., 1986a, *Nature*, **324**, 446  
 Barnes J., Hut P., 1986b, *nature*, **324**, 446  
 Barnes D. J., Henson M. A., Kay S. T., McCarthy I. G., Bahe Y. M., Eagle Collaboration 2015, p. 41  
 Barnes D. J., Kay S. T., Henson M. A., McCarthy I. G., Schaye J., Jenkins A., 2017, *MNRAS*, **465**, 213  
 Baugh C. M., Efstathiou G., 1994, *MNRAS*, **267**, 323  
 Behroozi P. S., Wechsler R. H., Wu H.-Y., 2013, *Astrophysical Journal*, **762**, 109  
 Beutler F., et al., 2011, *MNRAS*, **416**, 3017  
 Blumenthal G. R., Faber S. M., Primack J. R., Rees M. J., 1984, *Nature*, **311**, 517  
 Bond J. R., Kofman L., Pogosyan D., 1996, *Nature*, **380**, 603  
 Booth C. M., Schaye J., 2009, *MNRAS*, **398**, 53  
 Cañas R., Elahi P. J., Welker C., del P Lagos C., Power C., Dubois Y., Pichon C., 2019, *MNRAS*, **482**, 2039  
 Carlberg R. G., Yee H. K. C., Ellingson E., 1997, *Astrophysical Journal*, **478**, 462  
 Chernyagin S., Lezhnin K., 2015, *Journal of Applied Mathematics and Physics*, **3**, 124  
 Colless M., et al., 2001, *MNRAS*, **328**, 1039  
 Cooperstock F. I., Faraoni V., Vollick D. N., 1998, *Astrophysical Journal*, **503**, 61  
 Cramer W. J., Kenney J. D. P., Sun M., Crowl H., Yagi M., Jáchym P., Roediger E., Waldron W., 2018, arXiv e-prints, p. arXiv:1811.04916  
 Dalla Vecchia C., Schaye J., 2008, *MNRAS*, **387**, 1431  
 Davis M., Peebles P. J. E., 1983, *Astrophysical Journal*, **267**, 465  
 Davis M., Efstathiou G., Frenk C. S., White S. D. M., 1985, *Astrophysical Journal*, **292**, 371  
 De Boni C., Böhringer H., Chon G., Dolag K., 2018, *MNRAS*, **478**, 2086  
 De Lucia G., Kauffmann G., Springel V., White S. D. M., Lanzoni B., Stoehr F., Tormen G., Yoshida N., 2004, *MNRAS*, **348**, 333  
 Dehnen W., Read J. I., 2011, *European Physical Journal Plus*, **126**, 55  
 Di Mascolo L., Churazov E., Mroczkowski T., 2018, arXiv e-prints, p. arXiv:1812.01034  
 Dolag K., Vazza F., Brunetti G., Tormen G., 2005, *MNRAS*, **364**, 753  
 Dolag K., Borgani S., Murante G., Springel V., 2009, *MNRAS*, **399**, 497  
 Doroshkevich A. G., Shandarin S. F., Zeldovich I. B., 1983, in Abell G. O., Chincarini G., eds, Vol. 104, Early Evolution of the Universe and its Present Structure. pp 387–391  
 Dressler A., Shectman S. A., 1988, *Astronomical Journal*, **95**, 985  
 Edge A. C., Stewart G. C., Fabian A. C., Arnaud K. A., 1990, *MNRAS*, **245**, 559  
 Efstathiou G., Frenk C. S., White S. D. M., Davis M., 1988, *MNRAS*, **235**, 715  
 Evrard A. E., 1988, *MNRAS*, **235**, 911  
 Fitchett M., Webster R., 1987, *Astrophysical Journal*, **317**, 653  
 Fukushige T., Makino J., 2001, *Astrophysical Journal*,

- 557, 533
- Ghigna S., Moore B., Governato F., Lake G., Quinn T., Stadel J., 2000, *Astrophysical Journal*, **544**, 616
- Gifford D., Miller C., Kern N., 2013, *Astrophysical Journal*, **773**, 116
- Gill S. P. D., Knebe A., Gibson B. K., 2005, *MNRAS*, **356**, 1327
- Hayward C. C., Torrey P., Springel V., Hernquist L., Vogelsberger M., 2014, *MNRAS*, **442**, 1992
- Henson M. A., Barnes D. J., Kay S. T., McCarthy I. G., Schaye J., 2017, *MNRAS*, **465**, 3361
- Hernquist L., Katz N., 1989, *The Astrophysical Journal Supplement Series*, **70**, 419
- Jauzac M., et al., 2018, *MNRAS*, **481**, 2901
- Jenkins A., Frenk C. S., White S. D. M., Colberg J. M., Cole S., Evrard A. E., Couchman H. M. P., Yoshida N., 2001, *MNRAS*, **321**, 372
- Jernigan J. G., Porter D. H., 1989, *The Astrophysical Journal Supplement Series*, **71**, 871
- Katz N., White S. D. M., 1993, *Astrophysical Journal*, **412**, 455
- Katz N., Weinberg D. H., Hernquist L., 1996, *The Astrophysical Journal Supplement Series*, **105**, 19
- Kay S. T., Thomas P. A., Jenkins A., Pearce F. R., 2004, *MNRAS*, **355**, 1091
- Kompaneets D. A., Lukash V. N., Novikov I. D., 1981, Presented at the Conf. on Origin of the Struct. of the Universe, Tallin, 6-10 Apr. 1981, **82**, 18090
- Kustaantneimo P., Stiefel E., 1965, *J. Math. Bd*, **218**, 27
- Le Brun A. M. C., McCarthy I. G., Schaye J., Ponman T. J., 2014, *MNRAS*, **441**, 1270
- Lopes P. A. A., Trevisan M., Laganá T. F., Durret F., Ribeiro A. L. B., Rembold S. B., 2018, *MNRAS*, **478**, 5473
- Mayet F., et al., 2017, arXiv e-prints, p. arXiv:1709.01255
- McCarthy I. G., Schaye J., Bird S., Le Brun A. M. C., 2017, *MNRAS*, **465**, 2936
- Mikkola S., Tanikawa K., 1999a, *Celestial Mechanics and Dynamical Astronomy*, **74**, 287
- Mikkola S., Tanikawa K., 1999b, *MNRAS*, **310**, 745
- Monaghan J. J., Lattanzio J. C., 1985, *Astronomy and astrophysics*, **149**, 135
- Monfardini A., et al., 2010, *Astronomy and Astrophysics*, **521**, A29
- Moore B., Ghigna S., Governato F., Lake G., Quinn T., Stadel J., Tozzi P., 1999, *Astrophysical Journal*, **524**, L19
- Navarro J. F., Frenk C. S., White S. D. M., 1997, *Astrophysical Journal*, **490**, 493
- Nurmi P., Heinämäki P., Saar E., Einasto M., Holopainen J., Martínez V. J., Einasto J., 2006, arXiv e-prints, pp astro-ph/0611941
- Okabe N., Futamase T., Kajisawa M., Kuroshima R., 2014, *Astrophysical Journal*, **784**, 90
- Onions J., et al., 2012, *MNRAS*, **423**, 1200
- Pandge M. B., Monteiro-Oliveira R., Bagchi J., Simionescu A., Limousin M., Raychaudhury S., 2019, *MNRAS*, **482**, 5093
- Peacock J. A., et al., 2001, *Nature*, **410**, 169
- Peebles P. J. E., 1980, *The large-scale structure of the universe*. Princeton university press
- Peters C. F., 1968, PhD thesis, Yale University.
- Planck Collaboration et al., 2014b
- Planck Collaboration et al., 2014a
- Planck Collaboration et al., 2018, arXiv e-prints, p. arXiv:1807.06209
- Planelles S., Borgani S., Dolag K., Ettori S., Fabjan D., Murante G., Tornatore L., 2013, *MNRAS*, **431**, 1487
- Plazas A. A., Meneghetti M., Maturi M., Rhodes J., 2019, *MNRAS*, **482**, 2823
- Plummer H. C., 1911, *Monthly notices of the royal astronomical society*, **71**, 460
- Porter D. H., 1985, PhD thesis, California Univ., Berkeley.
- Power C., Navarro J. F., Jenkins A., Frenk C. S., White S. D. M., Springel V., Stadel J., Quinn T., 2003, *MNRAS*, **338**, 14
- Prat J., et al., 2018, *Physical Review D*, **98**, 042005
- Press W. H., Schechter P., 1974, *Astrophysical Journal*, **187**, 425
- Sayers J., et al., 2013, *Astrophysical Journal*, **778**, 52
- Schaye J., Dalla Vecchia C., 2008, *MNRAS*, **383**, 1210
- Schaye J., et al., 2010, *MNRAS*, **402**, 1536
- Springel V., 2000, *MNRAS*, **312**, 859
- Springel V., 2005, *MNRAS*, **364**, 1105
- Springel V., Yoshida N., White S. D. M., 2001a, *New Astronomy*, **6**, 79
- Springel V., White S. D. M., Tormen G., Kauffmann G., 2001b, *MNRAS*, **328**, 726
- Stoehr F., White S. D. M., Tormen G., Springel V., 2002, *MNRAS*, **335**, L84
- Tormen G., Bouchet F. R., White S. D. M., 1997, *MNRAS*, **286**, 865
- Tweed D., Devriendt J., Blaizot J., Colombi S., Slyz A., 2009, *Astronomy and Astrophysics*, **506**, 647
- Vikhlinin A., et al., 2009, *Astrophysical Journal*, **692**, 1060
- Vollmer B., Cayatte V., Balkowski C., Duschl W. J., 2001, *Astrophysical Journal*, **561**, 708
- Wechsler R. H., Bullock J. S., Primack J. R., Kravtsov A. V., Dekel A., 2002, *Astrophysical Journal*, **568**, 52
- White M., 2014, *MNRAS*, **439**, 3630
- White S. D. M., Frenk C. S., 1991, *Astrophysical Journal*, **379**, 52
- Yoshida N., Abel T., Hernquist L., Sugiyama N., 2003, *Astrophysical Journal*, **592**, 645
- Zel'dovich Y. B., 1970, *Astronomy and astrophysics*, **5**, 84
- Zwicky F., 1933, *Helvetica Physica Acta*, **6**, 110
- van Albada G. B., 1961, *Astronomical Journal*, **66**, 590
- von Hoerner S., 1960, *Zeitschrift fur Astrophysik*, **50**, 184

This document has been typeset from a *TEX/La<sup>t</sup>E<sub>X</sub>* file prepared by the author.